RSC Advances

REVIEW

View Article Online
View Journal | View Issue

Cite this: *RSC Adv.*, 2025, **15**, 40687

Next-generation cobalt hybrid material: structural, luminescence, and dielectric properties for advanced functional applications

Hajer Khachroum, *[ab] Abdallah Ben Rhaiem, [d] Mohammed S. M. Abdelbaky, [bc] Santiago García-Granda [b] and Mohamed Dammak[a]

Significant attention has been devoted to the development of a unique cobalt-based hybrid material with intriguing structural properties. In this study, we successfully synthesized a new hybrid compound *via* slow evaporation at room temperature. The compound was thoroughly characterized using single-crystal and powder X-ray diffraction (SXRD and PXRD), scanning electron microscopy (SEM), thermal analysis (DSC and TG/DTA), Fourier transform infrared (FT-IR) spectroscopy, and photoluminescence (PL) spectroscopy. X-ray diffraction analysis revealed that the zero-dimensional hybrid compound $[(C_6H_5N_2)_2CoCl_4]$ crystallizes in the tetragonal $P4_1$ space group, with the unit cell parameters $a = b =$ 6.8311 (3) Å, $c =$ 36.092 (3) Å, $\alpha = \beta = \gamma = 90°$, and $Z = 4$. The structure is stabilized by an extensive network of hydrogen bonds and π–π interactions, which connect the organic and inorganic components, forming a three-dimensional framework. FT-IR spectroscopy confirmed the presence of all expected vibrational modes. SEM analysis, combined with EDX, verified the presence of all non-hydrogen elements. Thermal analysis showed that the compound is thermally stable up to 380 K. PL spectroscopy demonstrated that the material exhibits blue-green emission, indicative of a charge-transfer process. The AC conductivity behavior was modeled using Jonscher's power law, confirming that the conduction process is thermally activated within the studied frequency range. The temperature dependence of the frequency exponent suggests that both the non-overlapping small polaron tunneling (NSPT) and correlated barrier hopping (CBH) mechanisms contribute to electrical conduction. Impedance spectroscopy of the real part of the dielectric permittivity showed a high dielectric constant at low frequencies, suggesting contributions from space charge accumulation and dipolar orientation. Additionally, the modulus spectra displayed two distinct relaxation peaks, corresponding to the grain and grain boundary effects.

Received 30th September 2025
Accepted 30th September 2025

DOI: 10.1039/d5ra07430d

rsc.li/rsc-advances

1. Introduction

Over the last decades, researchers have devoted substantial attention to hybrid organic–inorganic materials (HOIMs) due to their unique structural properties as well as the wide range of prospective applications they offer across various fields, including electronics, optics, semiconductors, conductors and materials science.[1–11] The increasing awareness of these materials stems from their ability to integrate the versatility of organic molecules with the stability of inorganic frameworks, resulting in fascinating structural and physical features such as ferroelectricity, ferro-elasticity, magnetic properties, optical properties, antibacterial activity, and photoluminescence.[12–24] In this case, we specialize in synthesising the hybrid compound expressed by the general formula $R_2[MX_4]$ (where R is a monovalent organic cation; M is a bivalent transition metal; and X is Cl, F, Br, or I). Particularly, the cobalt(II)-based materials were discovered to have intriguing magnetic, electrical, optical, thermal stability and structural properties,[25–31] revealing significant promise for use in developing revolutionary materials for technological, energy, and industrial applications. In addition, an assortment of organic–inorganic structures that hold 4-cyanopyridine cations have been published in the literature, including $[C_6N_2H_5]_3BiCl_6$, $[(C_6H_5N_2)_2ZnCl_4]$, and $[MX_2(4\text{-}CNpy)_x]_n$.[32–34] These mixtures are especially noteworthy since they possess distinctive characteristics, including nonlinear optical activity, semiconductor behaviour, ferroelectric and magnetic properties. For this purpose, we report the synthesis of a new hybrid complex based on cobalt cation, formulated as

[a]*Laboratory Inorganic Chemistry, Faculty of Sciences of Sfax, University of Sfax, 3000 Sfax, Tunisia. E-mail: khachroum.hajer2015@gmail.com*

[b]*Departamento de Química Física y Analítica, Universidad de Oviedo-CINN, 33006 Oviedo, Spain*

[c]*Departamento de Química Física, Facultad de Ciencias Químicas, Universidad de Salamanca, E-37008 Salamanca, Spain*

[d]*Laboratory LaSCOM, Faculty of Sciences of Sfax, University of Sfax, BP1171, 3000 Sfax, Tunisia*

$(C_6H_5N_2)_2CoCl_4$, and discuss its crystal structure, vibrational analysis, and thermal behaviour. The photoluminescence properties are also discussed.

2. Experimental details

2.1. Synthesis

2.1.1. Preparation of $(C_6H_5N_2)_2CoCl_4$. The organic–inorganic hybrid material was prepared by slow evaporation at room temperature from a mixture of an aqueous solution of 4-cyanopyridine (2 mmol, 0.209 g, 99.99% purity, Sigma-Aldrich) diluted in 6 mL of purified water, which was added to a solution of $CoCl_2 \cdot 6H_2O$ (0.237 g, 98% purity, Sigma-Aldrich) dissolved in 2 mL of distilled water. The resulting solution was stirred for 30 minutes at room temperature (298 K) using a magnetic stirrer. After stirring, the clear solution was poured into a 100 mL glass beaker, which was then loosely covered with perforated parafilm to allow for slow evaporation. The beaker was kept undisturbed at room temperature (298 K) for a few days to allow for crystal growth. No stirring or agitation was applied during this period. Single violet crystals were obtained and used for the characterization study.

2.2. Characterization

2.2.1. X-ray single-crystal structural analysis. For structural analysis, a bluish single crystal with dimensions of 0.12 × 0.17 × 0.05 mm^3 was carefully selected under a microscope and mounted on a Mitogen micromesh using a small amount of mineral oil. Diffraction data were collected at room temperature on an Agilent Gemini CCD diffractometer equipped with a graphite-monochromated Mo-Kα radiation source (λ = 0.71073 Å). The structure was solved using the direct methods implemented in the SIR2014 program[35] within the WinGX package.[36] Empirical absorption corrections were applied based on multiple scans. Structure refinement was carried out using Olex2.1 (ref. 37) with SHELXL.[38] All non-hydrogen atoms were located from successive Fourier difference maps and refined anisotropically. The hydrogen-atom positions were calculated geometrically and refined using a riding model. Molecular graphics were prepared using Mercury and DIAMOND software[39,40] to visualize the crystal compound. The selected crystallographic data and experimental conditions are summarized in Table 1. The atomic coordinates and equivalent isotropic displacement parameters are given in Table S1, bond lengths and angles in Table S2, and anisotropic displacement parameters in Table S3.

2.2.2. Morphology and purity analysis. Powder X-ray diffraction measurements were carried out using a Siemens D5000 diffractometer equipped with a Cu-Kα radiation source (λ = 1.5406 Å). Before the measurement, several single crystals of the compound were carefully ground into a fine powder using an agate mortar to minimize preferred orientation effects. Data were collected in the 2θ range of 10–50°, with a step size of 0.02° and a counting time of 1 s per step. The instrument was operated at 40 kV and 4 mA. As demonstrated in Fig. 1, the obtained diffraction pattern was compared with the simulated pattern calculated from the single-crystal X-ray diffraction data, confirming that the synthesized material was obtained as a pure crystalline phase.

Table 1 Crystal data and structure refinement for the title compound $(C_6H_5N_2)_2CoCl_4$

Formula	$(C_6H_5N_2)_2CoCl_4$
Formula weight (g mol^{-1})	410.97
T (K)	293
Crystal system	Tetragonal
Space group	$P4_1$
Unit cell dimensions	$a = b = 6.8311$ (2) Å
	$c = 36.092$ (3) Å
	$V = 1684.21$ (16) $Å^3$
Z	4
D_x (g cm^{-3})	1.613
2θ range for data collection (°)	4.998–62.85
μ (mm^{-1})	1.649
F (000)	812.0
Crystal size/mm^3	0.21 × 0.17 × 0.05
hkl range	$-10 \le h \le 10$
	$-10 \le k \le 10$
	$-52 \le l \le 52$
Data collection instrument	Kappa CCD
Wavelength (Å)	0.71073
Measured reflections	12 193
Observed reflections ($I > 2\sigma(I)$)	2609
R indices	$R_1 = 0.07$; w$R_2 = 0.08$
Goodness-of-fit on (F^2)	0.953
Highest peak/deepest hole (e $Å^{-3}$)	$-0.66 < \Delta\rho < 0.41$
CCDC deposition number	2281873

2.2.3. Scanning electron microscopy analysis. SEM micrographs and energy-dispersive X-ray spectroscopy (SEM/EDX) were conducted using a JEOL-6610LV scanning electron microscope, operating at 20 kV, coupled with an Oxford X-Max microanalysis system (EDX). For clearer images, small samples were coated with a thin gold layer before taking the pictures.

2.2.4. FT-IR spectroscopy analysis. At room temperature, infrared spectra were collected with a Bruker Tensor-27 FT-IR

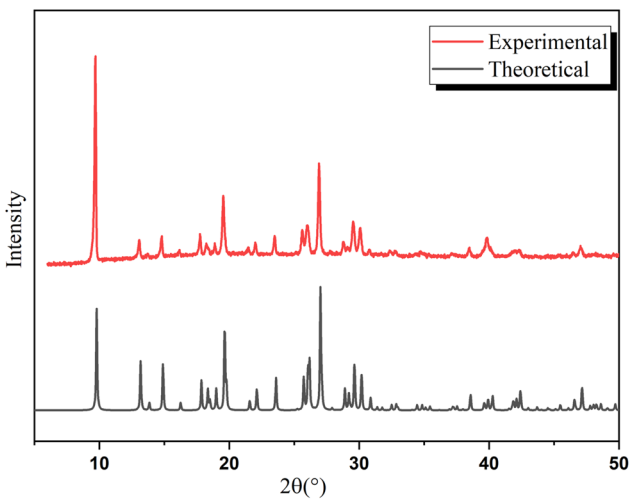

Fig. 1 Superposition of the theoretical and experimental patterns at room temperature.

spectrometer. The samples were produced as KBr pellets (about 1 mg of sample finely crushed with 200 mg of dry KBr) and vacuum-pressed into 13 mm discs. The spectra were obtained in the 4000–400 cm^{-1} range, with an average of 15 scans per sample and a resolution of 4 cm^{-1}.

2.2.5. Thermal analysis. Differential scanning calorimetry (DSC) of the two samples was conducted using the SETARAMDSC131 ks instrument at temperatures ranging from 300 to 850 K, at a heating rate 10 K min^{-1}. TG/DTA were performed using the TGA Q500 TA instrument. The powder sample (m = 12.835 mg) of the investigated material was heated from 300 to 950 K at a heating rate of 10 K min^{-1} in a nitrogen atmosphere.

2.2.6. Photoluminescence spectra. The photoluminescence excitation (PLE) and photoluminescence (PL) spectra were recorded at room temperature on a PerkinElmer LS-55 spectrometer with an attachment for solid-state measurements.

2.2.7. Electrical measurements. The electrical impedance of a 1 mm-thick, 8 mm^2 surface area wafer was determined using a Solartron SI 1260 instrument at 1 V AC. The measurements were carried out in air over a frequency range of 0.1 Hz to 10 MHz and at temperatures ranging from 313 K to 403 K. Two thin silver-plated copper wires served as electrical contacts on the wafer surface, which was also silver-plated to improve the measurement accuracy. This configuration enabled accurate impedance data collection within the defined temperature and frequency ranges.

3. Results and discussion

3.1. Crystal structure description

The single crystal X-ray diffraction analysis shows that this material has the formula of $(C_6H_5N_2)_2$ $CoCl_4$. It belongs to the tetragonal system with the non-centrosymmetric $P4_1$ space group. The unit cell parameters are as follows: $a = b = 6.8311$ (3) Å, c = 36.092 (3) Å, $\alpha = \beta = \gamma = 90°$ and Z = 4. Indeed, as illustrated in Fig. 2, the asymmetric unit consists of one $[CoCl_4]^{2-}$ inorganic anion and two protonated $(C_6H_5N_2)^+$ organic cations. The cobalt atom has a +II oxidation state, presenting as Co^{2+}.

The crystal structure is composed of tetrahedral inorganic $[CoCl_4]^{2-}$ anions alternating with monovalent organic cations $(C_6H_5N_2)^+$ along the c-axis in such a way that the negative charge of $[CoCl_4]^{2-}$ is compensated with the positive charge of the two $(C_6H_5N_2)^+$ cations (see Fig. 3).

In fact, the tetrahedral cobalt cation, Co^{2+}, is surrounded by four chlorine atoms with Co–Cl distances ranging from 2.257 (2) to 2.292 (17) Å, with Cl–Co–Cl angles varying from 105.92 (8)° to 117.79 (13)°. The $[CoCl_4]^{2-}$ tetrahedron shows a slight distortion, as proven in the literature.[41–43] The organic cations can adopt various orientations along the c-axis. The C–C and C–N bond lengths are in the ranges of 1.34 (2) to 1.45 (22) Å and 1.120 (16) Å to 1.35 (2) Å, forming C–N–C and N–C–C bond angles balancing from of 121.2 (15)° to 124.7 (16)° and 119.0 (16)° to 119.6 (6)°, respectively. These outcomes are analogous to those obtained in complexes incorporating 4-cyanopyridine as the organic framework.[30,41–43] Additionally, the cohesion of the crystal structure is concluded by the existence of five types of hydrogen-bond interactions between the organic cations and the inorganic anions: N1–H1···Cl4(i), N3–H2···Cl2(ii), C4–H4···Cl1(i), C8–H8···Cl3, and C9–H9···Cl3(ii).[44–46] The N–Cl lengths are in the range of 3.11 (13) Å, forming N–H···Cl bond angles that vary from 161° to 168°. Conversely, the C–Cl distances fluctuate between 3.47 (2) Å and 3.664 (15) Å, generating C–H···Cl bonds with angles spanning from 146° to 153°. Table 2 highlights the hydrogen interaction outcomes. The title compound's structure is stable owing to π–π stacking interactions between a plane containing bonded aromatic rings with a laminate distance of 3.582 (3) Å, which is comparable to interplanar spacing in aromatic π systems.

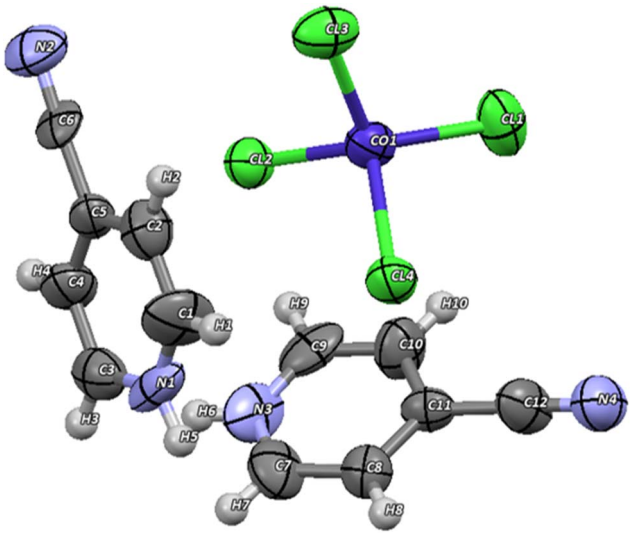

Fig. 2 Perspective view of the asymmetric unit of $(C_6H_5N_2)_2CoCl_4$ at the 50% probability ellipsoid.

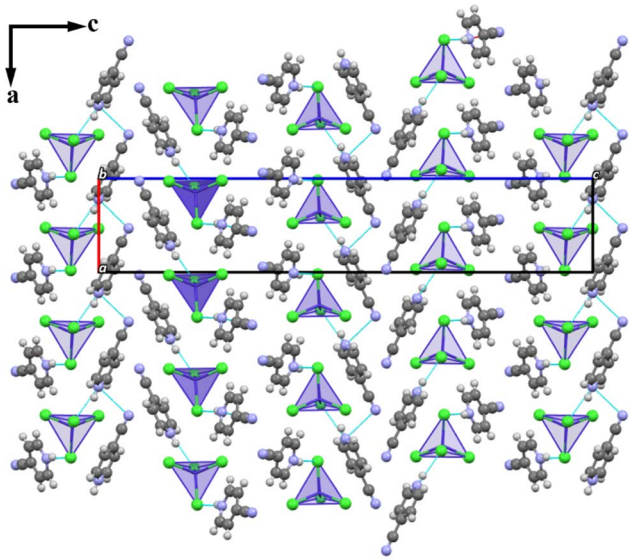

Fig. 3 Projection of the packing arrangement of $(C_6H_5N_2)_2CoCl_4$ in the plane (a and c) showing hydrogen bonds.

Table 2 Hydrogen bonds of compound (1)[a]

D—H···A	D—H (Å)	H···A (Å)	D···A (Å)	D—H···A (°)
N1–H1···Cl4(i)	0.86	2.29	3.119 (14)	161
N3–H2···Cl2(2i)	0.86	2.27	3.11 (13)	168
C4–H4···Cl1(i)	0.93	2.66	3.47 (2)	146
C8–H8···Cl3	0.93	2.81	3.664 (15)	153
C9–H9···Cl3(2i)	0.93	2.69	3.506 (18)	147

[a] Symmetry codes: (i) y, $1-x$, $-\frac{1}{4}+z$; (2i) $1+x$, $-1+y$, z.

3.2. Surface characterization by SEM/EDX

The shape component of the new hybrid compound can be seen *via* SEM analysis coupled with EDX spectroscopy. As mentioned in Fig. 4(a–c), the average size of the particles was between 10 and 200 μm. According to these results, it seems that the particles on the surface grow with a similar morphology and some agglomerated particles. The EDX spectrum presented in Fig. 4(f), covering the 0–30 keV range, verifies the presence of all the non-hydrogen elements with intensity peaks of C: 57.68%, N: 19.10%, Cl: 19.29% and Co: 3.83%. However, the EDX spectrum (Fig. 4(e)) recorded in the range of 0–10 keV reveals the presence of oxygen, which may be attributed to impurities.

3.3. FT-IR spectroscopy analysis

The FT-IR spectrum of the structural compound in the frequency region of 400–4000 cm^{-1} is depicted in Fig. 5. In the high-frequency region (3500–3200 cm^{-1}), the symmetric and asymmetric stretchings of the N–H bonds are projected at 3553, 3484 and 3409 cm^{-1}.[47,48] The bands detected at 3228 and 2910 cm^{-1} are attributed to the C–H stretching modes. However, the small peaks detected at 2289 and 2228 cm^{-1} refer to the (C≡N) stretching vibration of the pyridine ring.[49–51] In fact, the intense peaks observed between 1615 and 1510 cm^{-1} are related to the valence vibration of ν(C=C). However, the bands observed at 1419–1220 cm^{-1} can be assigned to the C–H deformation in the methylene group and the scissoring modes of γ(C–C). In the law frequency region, the peaks detected between 1064 and 470 cm^{-1} are attributed to the out-of-plane

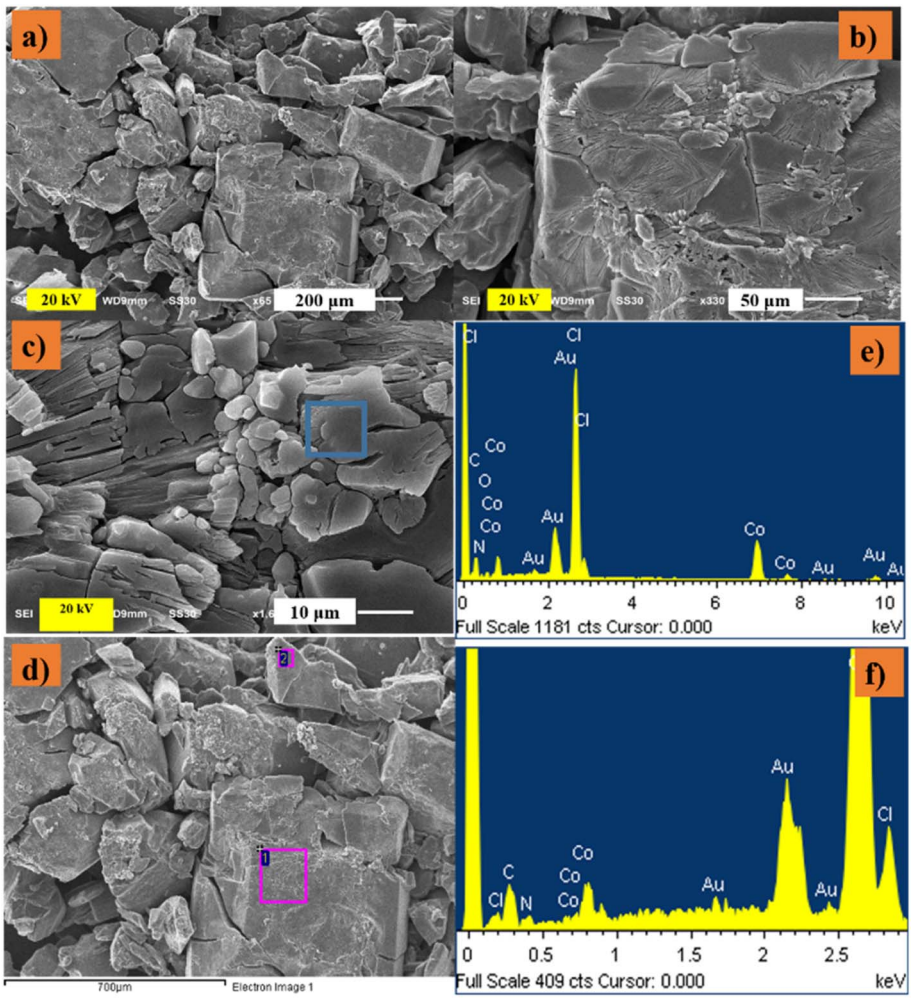

Fig. 4 SEM images (a–d) and (e and f) EDX spectra from 0 to 10 k eV and from 0 to 30 keV, respectively, of $(C_6H_5N_2)_2CoCl_4$ crystals grown by slow evaporation at room temperature.

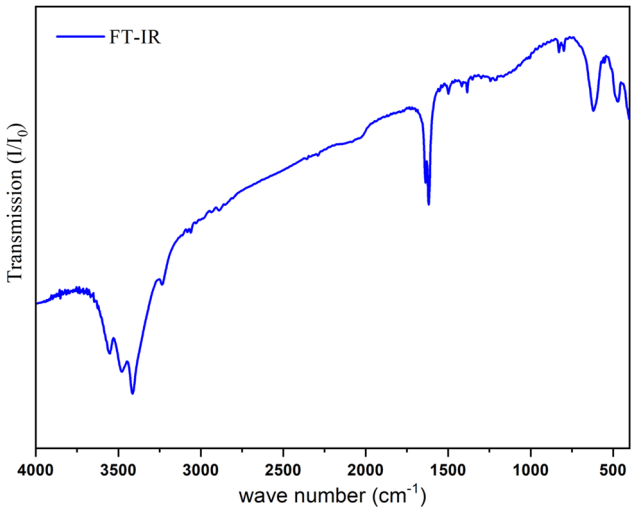

Fig. 5 FT-IR spectrum of $(C_6H_5N_2)_2$ $CoCl_4$ at room temperature.

deformation modes of C–H and the deformation vibrations of C–C. All these assignments are in good agreement with those reported for some previous compounds.[52–54]

3.4. Thermal decomposition

The thermal behavior was investigated from simultaneous TG/DTA curves and DSC traces, as depicted in Fig. 6(a and b), respectively.

The anhydrous compound shows thermal stability up to 450 K, beyond which it decays in three successive steps, losing 73.74% (observed) and 75.98% (calculated) of its total weight. The first and second steps occurred between 440 and 797 K, where it lost 52.56% (observed) and 51.10% (calculated), corresponding to the loss of the two organic entities, which is accompanied by the endothermic peaks in the DTA curve at 497 K and 789 K.[55,56] Also, the two endothermic peaks detected in the DSC curve at 470 K and 756 K affirm this decomposition. The last weight loss took place at 797 K, where it lost approximately 21.18% (observed) and 24.88% (calculated) of its total weight, which can be attributed to the release of the inorganic part. This transformation is accompanied by two endothermic peaks in the DTA and DSC curves at 812 K and 808 K, respectively.[57] Finally, a residue of 26.26% (observed) and 25.37% (calculated) was obtained from the compound $(C_6H_5N_2)_2CoCl_4$, corresponding to the formation of cobalt (II) monoxide (CoO).

3.5. Photoluminescence analysis

The photoluminescence excitation (PLE) and photoluminescence emission (PL) spectra are depicted in Fig. 7. In the PLE spectrum, three distinct peaks at 371 nm, 389 nm, and 434 nm are observed in the 300–454 nm range. Since the absorption peak at 389 nm is more intense than the other

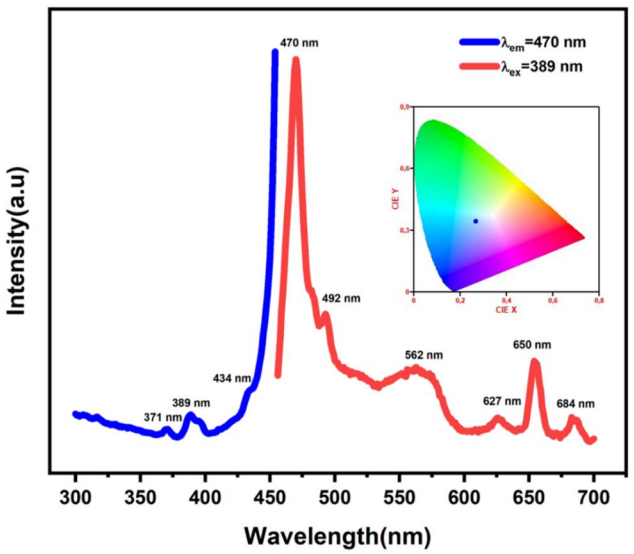

Fig. 7 Photoluminescence excitation (PLE) and photoluminescence emission (PL) spectra of $(C_6H_5N_2)_2CoCl_4$.

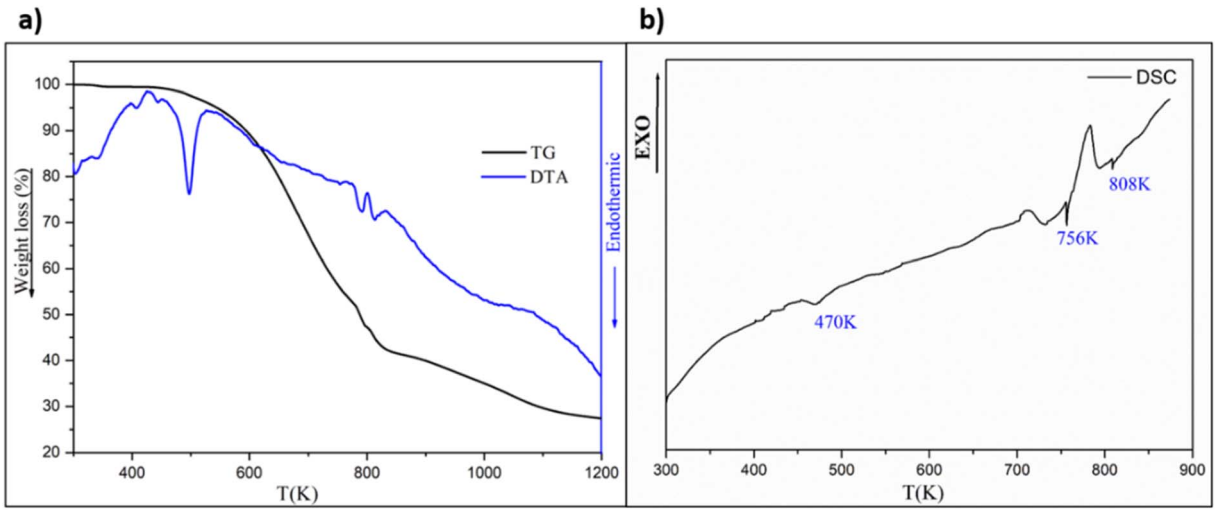

Fig. 6 (a) Simultaneous TG/DTA curves and (b) DSC curve of $(C_6H_5N_2)_2CoCl_4$ in a N_2 atmosphere.

absorption peaks, the Near UV LED chip can effectively excite the synthesized compound. The PL emission spectra measured at 389 nm excitation reveal a series of peaks in the 456–700 nm wavelength region. A total of six emission bands exists. The chromaticity diagram (inset Fig. 7) reveals that the investigated compound displays a vibrant blue-green emission at a wavelength of λ_{ex} = 389 nm, according to the International Commission on Illumination (CIE) standard. The luminescent peaks detected at 371, 389 and 434 nm in the PLE spectrum may originate from the n → π* and π → π* transitions that occur between 4-cyanopyridinium cations and the excited state.[58–60] Furthermore, the existence of an anionic species significantly impacts the electronic characteristics, thereby influencing both the color and intensity of emission. Additionally, these molecular hybrids can be tailored by choosing diverse molecular building blocks that interact to yield particular optical properties. However, the emission spectra reveal a series of peaks, corresponding to three spin-allowed d–d electronic alterations within the $[CoCl_4]^{2-}$ anions, in line with the crystal field theory. The two emission peaks at 470 and 492 nm are assigned to the ligand-to-metal charge transfer. However, the emission peak observed at 562 nm is attributed to the $^4A_2(F) \rightarrow {}^4T_1(^4P)$ transition. Additionally, the $^4A_2(F) \rightarrow {}^4T_1(^4F)$ transition of the electrons can be detected at around 627 nm. The last two emission peaks at 650 and 684 nm correspond to the $^4A_2(F) \rightarrow {}^4T_2(^4F)$ transition. These obtained results are similar to those observed for some hybrid compounds using tetrachlorocobaltate,[61–67] which confirms the validity of this model.

3.6. Temperature–frequency dependence of AC conductivity

To look into the dynamic reaction of a material in response to an alternating electric field, a study of the effect of alternating current (AC) conductivity was performed. AC measurements provide trustworthy details about the transport phenomenon in materials, as well as a glimpse into the location of the electric field and field-induced disruptions.

The real AC-conductivity spectrum illustrated in Fig. 7 displays two different dispersion zones. In the low-frequency domain, the AC conductivity shows a frequency-independent conductivity plateau (10^{-1} rads^{-1} < ω < 10^5 rads^{-1}), primarily due to its DC conductivity governed by the motion of charge carriers. Beyond the critical hopping frequency (ω_c), the conductivity, σ, increases sharply and almost linearly with frequency. This variation demonstrates that at high frequencies, charge carriers are no longer able to follow the electric field in the traditional manner, but instead respond with quick and dynamic sauts. The strong frequency dependence of conductivity reflects the activation of conduction mechanisms in which mobility is dependent on the frequency applied. The evolution of σ with frequency demonstrates the change from ohmic to dispersive transport, dominated by the dynamic response of the carriers. This common behaviour is characteristic of materials that conduct by means of sauts (Fig. 8).[68]

The investigated $(C_6H_5N_2)_2CoCl_4$ material demonstrates a conductivity value of (6×10^{-3} Ω^{-1} cm^{-1}) at 403 K, indicating

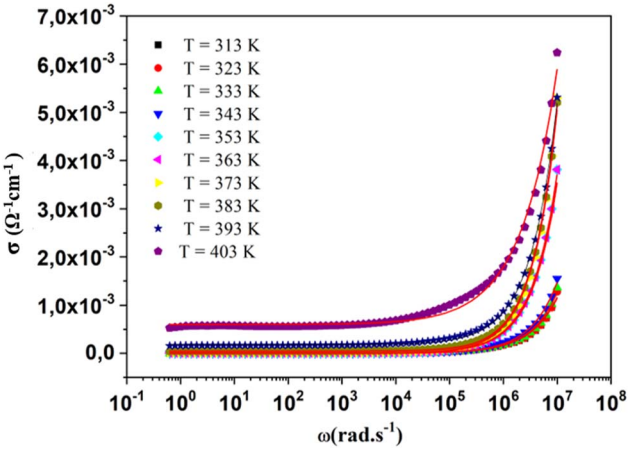

Fig. 8 Experimental and calculated (—) conductivity data for $(C_6H_5N_2)_2CoCl_4$ at different temperatures.

its characteristics as a semiconductor material in the temperature heating range.[69,70] Our investigated sample exhibits a greater value of conductivity compared with other similar compounds, such as $[(CH_3)_2NH_2]_2$ $CoCl_4$ (7×10^{-4} Ω^{-1} cm^{-1}).[71] This particular property holds promise for application in various devices, such as photovoltaics, optoelectronics, and photodetectors.[72,73] It seems that the AC conductivity obeys Jonscher's power law:[74]

$$\sigma_{ac} = \sigma_{dc} + A\omega^s \; 0 < s < 1 \quad (1)$$

In this equation, σ_{dc} defines the direct current conductivity, $\omega = 2\pi f$ represents angular frequency, A is a pre-exponential constant, and s reflects the percentage of contact between mobile ions and the surrounding lattice.

Furthermore, the temperature response of the exponent factor (s) can aid the identification of the conduction mechanism based on Eliott's behavior.

The temperature dependence of (s) is graphed in Fig. 9(a). It can be noted that the graph presents two phases, indicating that the conduction process can be manifested by two distinct models. In the first temperature region (313 K < T < 363 K), it can be seen that the values of the exponent factor (s) increase with the temperature; therefore, the (NSPT) model is applicable to the obtained results in this phase.[75,76] Conversely, in the second phase (T > 363 K), the value of (s) decreases with rising temperature, as established by the Correlated Barrier Hopping (CBH) model.[77,78]

Fig. 9(b) illustrates the variation in L_n ($\sigma_{dc}T$) *versus* reciprocal temperature (1000/T), obtained from power law fits of the AC conductivity. The current conductivity can be estimated using the Arrhenius law for thermally activated processes, as shown by the following relation:

$$\sigma_{dc}(T) = A \times \exp\left(-\frac{E_a}{K_B T}\right) \quad (2)$$

It should be noted that the Arrhenius plot of σ_{dc} demonstrates a change in the mechanism of conduction at 363 K.

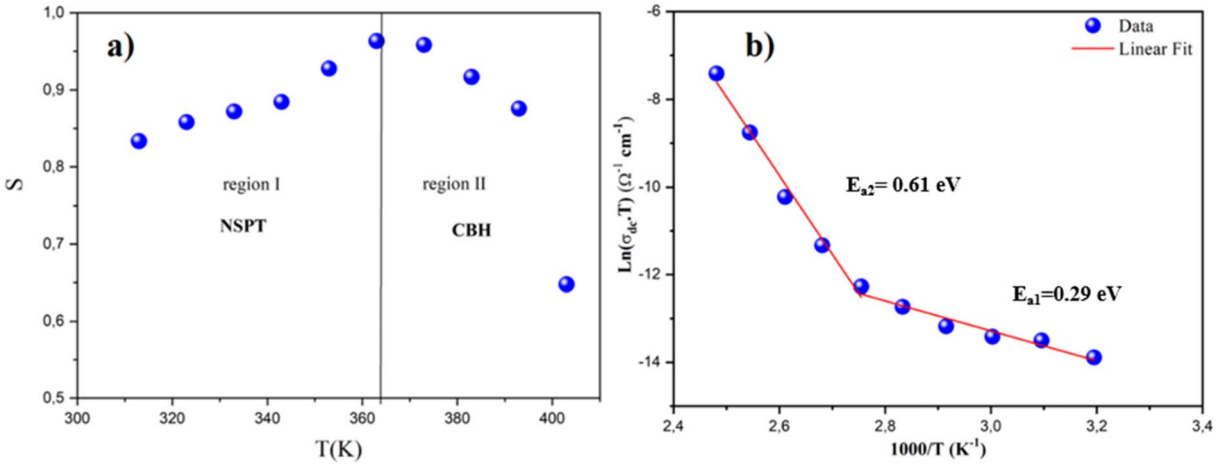

Fig. 9 (a) Temperature dependence of the exponent factor (S) *versus* 1000/T and (b) variation in L_n ($\sigma_{dc}T$) *versus* 1000/T.

Therefore, two regions are detected, accompanied by two activation energies. The first one is described by $E_{a1} = 0.29$ eV in the temperature range between 313 and 363 K, while the second region (363–403 K) is characterized by an activation energy value at $E_{a2} = 0.61$ eV. These features affirm that the conduction behavior was manifested by the two conduction models.

3.7. Frequency dependence of the dielectric permittivity

The complex permittivity of a material provides in-depth insights into the nuanced interplay between its chemical compositions and physical qualities as well as the intricate manifestations of its electrical and dielectric properties. The complex permittivity can be described by the following equation:

$$\varepsilon^*(\omega) = \varepsilon'(\omega) - j\varepsilon''(\omega) \quad (3)$$

where ε' is the capacity of the material to store energy, and ε'' represents the dissipation of energy in the material.

$$\varepsilon'(\omega) = \frac{Z''}{\omega C_0\left(Z'^2 + Z''^2\right)} \quad (4)$$

where $C_0 = \varepsilon_0 \times A/d$; C_0 is the vacuum capacitance; ε_0 is the vacuum dielectric constant; A and d are the surface and the thickness of the pad, respectively; Z' and Z'' are the real and the imaginary parts of the impedance, respectively; and ω is the angular frequency.

The frequency dependence of the capacitance ε' at various temperatures is illustrated in Fig. 10(a). Two distinct zones are observed in this frequency range. It is evident that ε' exhibits dispersion at low frequencies and becomes nearly constant at high frequencies. Ionic, electronic, interfacial, and orientational polarisations dominate the dielectric constant in the low-

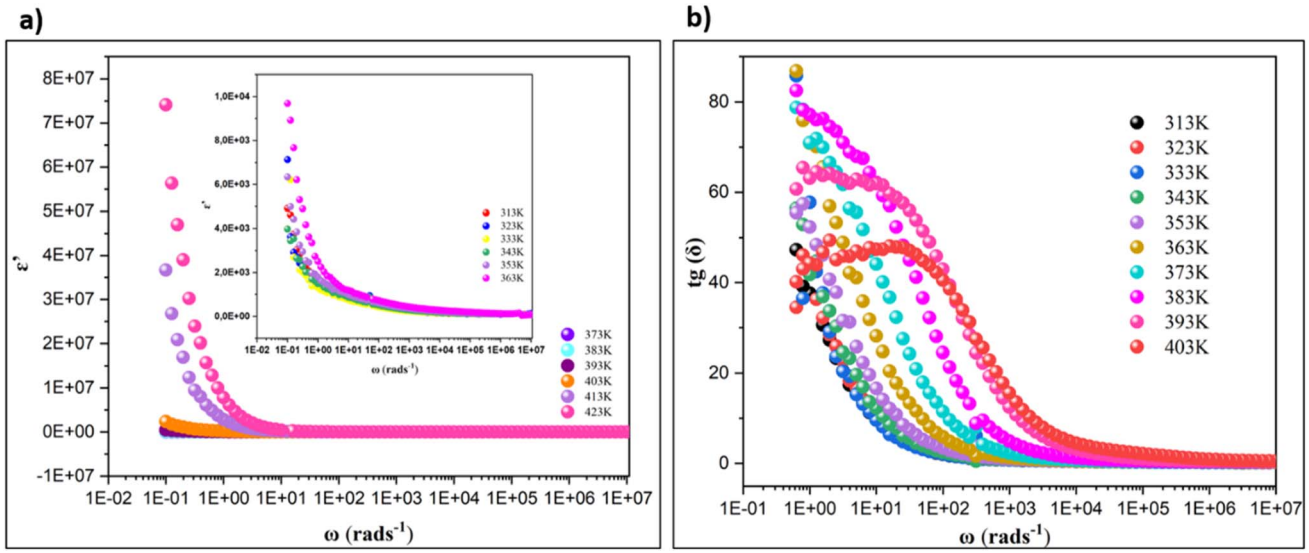

Fig. 10 (a) Frequency dependence of the dielectric constant at various temperatures and (b) frequency dependence of the dielectric loss factor t_g (δ) at various temperatures.

frequency region.[79–82] The observed variation in the real permittivity component with frequency is explained by the Maxwell–Wagner interfacial polarisation theory,[83] which corresponds to ion exchange among the same molecules during the polarisation process at interfaces, elucidating the non-Debye behaviour. Koop's phenomenological theory contributes to this explanation.[84] According to this concept, the substance is composed of conducting grains separated by weakly conducting grain boundaries.[85,86] These grain boundaries act as traps for charge carriers, restricting their motion. Consequently, interfacial polarization enables charge exchange or electron hopping between ions within the same molecular framework. When an electric field is provided, positive charges shift towards the negative pole and negative charges move towards the positive pole, resulting in dipoles. At low frequencies, space charges can travel to the grain boundary areas, but the high resistance causes them to accumulate, thereby increasing polarisation. At high frequencies, the quick shifting of the field prohibits further charge-carrier accumulation, hence lowering polarisation. This explains why the dielectric constant falls with increasing frequency. Temperature-sensitive orientational and interfacial polarisations dominate the material's electrical sensitivity at low frequencies.[87] The increase in permittivity (ε') with temperature is primarily caused by heat-activating charge carriers and the presence of molecular dipole moments.[88] It can be inferred that our investigated compound has a significant dielectric constant value as high as 7.5×10^7 compared with the values of other reported similar materials, such as $[C_6H_{10}(NH_3)_2]CoCl_4 \cdot H_2O$ ($\varepsilon' \approx 1.4 \times 10^6$),[89] $[C_9H_8NO]_2CoCl_4$ ($\varepsilon' \approx 150$)[31] and $[DMA]_2CoCl_4$ ($\varepsilon' \approx 0.5 \times 10^6$).[90]

Fig. 10(b) reveals the frequency dependence of the dissipation factor t_g (δ) at various temperatures from 313 K to 403 K, with the t_g values spanning 10^{-1} to 10^7 rad s^{-1}. In the current sample, the motion of the loss factor is significantly high in the low-frequency range. The movement of charge carriers is restricted by space-charge polarization, which confines partial conduction until charges accumulate at grain boundaries or barriers. The compound demonstrates two relaxation peaks at low and high frequencies, attributed to space charge and dipole polarization, respectively. The t_g (δ) value is notably high in the low-frequency range and decreases with increasing frequency. The restricted movement of charge carriers due to space-charge polarization in the low-frequency region demands additional energy, resulting in higher t_g (δ) values below 10^3 rad s^{-1}. As frequency increases, the resistivity decreases, reducing the energy required for charge-carrier movement and thereby lowering the dielectric loss in the high-frequency region. The highest motion of loss factor is primarily due to the influence of grain-boundary resistivity, which exceeds the contribution of the grain itself. Additionally, an increase in temperature causes t_g (δ) to rise further.

The title compound exhibits high dielectric permittivity and minimal dielectric loss, indicating its effectiveness in energy storage with reduced heat dissipation. These properties make it an excellent candidate for application in optoelectronics, such as capacitors and energy-storage systems. The material's low dielectric loss ensures efficient energy storage, making it well-suited for energy-conscious devices. Additionally, materials with elevated dielectric constants are valuable in devices, like dielectric gates or active channels in FETs. Notably, materials with low energy loss are essential for battery applications.[88,91]

3.8. Frequency dependence of dielectric modulus

The intricate electrical modulus serves as a vital instrument for examining electrical characteristics, especially dielectric relaxation. It accounts for most of the sample's reaction, all the while reducing the impact of blocking electrodes.

The imaginary portion of the electric modulus (M'') was derived using the following formula:[92]

$$M'' = \frac{\varepsilon''}{\varepsilon'^2 + \varepsilon''^2} \quad (5)$$

Fig. 11(a) depicts the frequency-dependent behavior of the imaginary component of the complex modulus (M'') at different temperatures. At low frequencies, M'' approaches zero, indicating limited electrode polarisation effects.[66] As frequency increases, M'' reaches an asymptotic maximum, indicating relaxation in the investigated material. As the temperature rises, the relaxation peaks shift to higher frequencies, demonstrating that the relaxation process is temperature-dependent. The asymmetric shape of the peaks indicates that the material does not exhibit Debye behavior.[93] The imaginary part M'' variation is divided into two regions: The low-frequency range ($\omega < \omega_{max} = 10^5$ rad s^{-1}) indicates the grain boundary relaxation, which is related to the long-distance charge-carrier motion. The second frequency region ($\omega > \omega_{max}$) only allows for localised motion, which corresponds to the grain relaxation. The relaxation peak indicates a shift in the charge-carrier mobility from long-range to localised behaviour.

The modulus spectra can be numerically simulated to discover charge-carrier features, like the activation energy and relaxation frequency. Bergman's proposed function describes the oscillation of the imaginary component of modulus M'' in the frequency range:[94]

$$M''(\omega) = \frac{M''_{1_{max}}}{(1-\beta_1) + \left(\frac{\beta_1}{1+\beta_1}\right)\left[\beta_1\left(\frac{\omega_{1_{max}}}{\omega}\right) + \left(\frac{\omega}{\omega_{1_{max}}}\right)^{\beta_1}\right]} + \frac{M''_{2_{max}}}{(1-\beta_2) + \left(\frac{\beta_2}{1+\beta_2}\right)\left[\beta_2\left(\frac{\omega_{2_{max}}}{\omega}\right) + \left(\frac{\omega}{\omega_{2_{max}}}\right)^{\beta_2}\right]} \quad (6)$$

where M''_{max} is the maximum peak; (ω_{max}), the peak angular frequency of the imaginary component of the modulus, and β were derived from the analysis. To account for the grain boundary effects, our experimental data were modelled using two Bergman functions. The measured values are well fitted to the prior equation.

The evolution of the maximum frequency linked to grain relaxation is examined by plotting L_n (ω_{max}) against the inverse of temperature, as shown in Fig. 11(b). This variation follows the Arrhenius plot, which is described by the following relation:

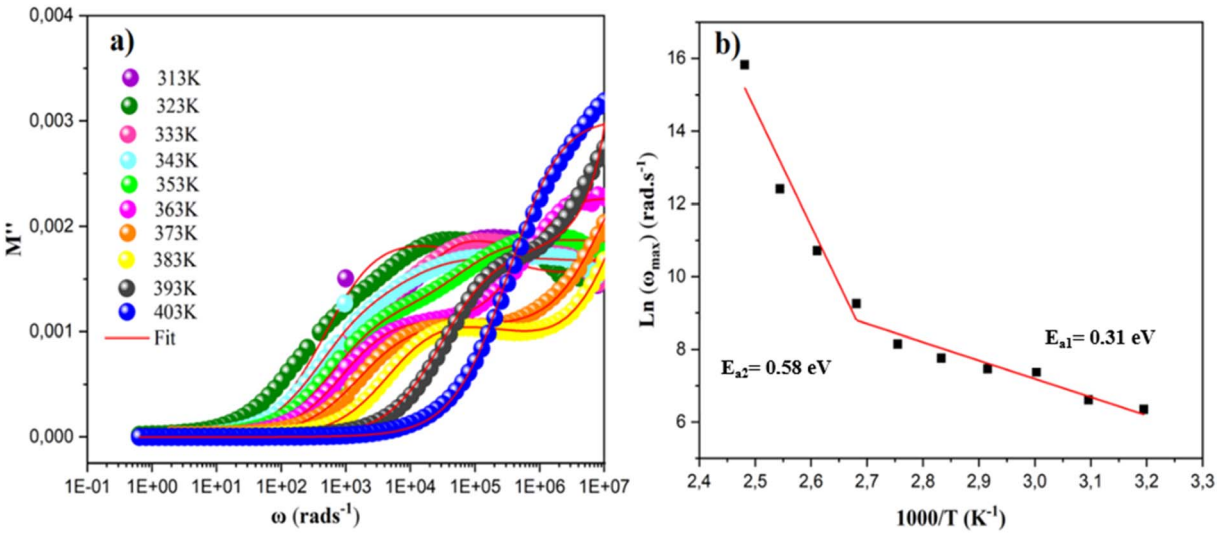

Fig. 11 (a) Variation of the imaginary part of the dielectric modulus at different temperatures and (b) temperature dependence of L_n (ω_{max}) *versus* 1000/*T*.

$$\omega_{max} = \omega_0 \times \exp\left(-\frac{E_a}{K_B T}\right) \quad (7)$$

The fitted curve reveals two relaxation regions manifested by a change of slope: the first relaxation is between 313 K and 363 K, with an activation energy of $E_{a1} = 0.31$ eV, and the second is obtained in the temperature range of 363 K to 403 K, with an activation energy of $E_{a2} = 0.58$ eV. The activation energies associated with the current conductivity and dielectric modulus are close. This suggests that the conduction and relaxation mechanisms are ensured by the same effect.

4. Conclusion

In conclusion, we have successfully synthesized unique cobalt-based organic–inorganic compounds using the slow evaporation method at room temperature. Our research has shown that a hybrid compound with the formula $(C_6H_5N_2)_2CoCl_4$ crystallizes in the tetragonal $P4_1$ space group. The crystal packing of this compound is stabilized by strong hydrogen bonds between $(C_6H_5N_2)^+$ and $[CoCl_4]^{2-}$ anions, as well as π–π interactions between the aromatic rings. The presence of functional groups in the organic moieties, as identified through structural investigations, is confirmed by FT-IR spectroscopy. By discussing the photoluminescence spectrum, it can be observed that the cobalt-based compound mentioned displays a vivid and vibrant relaxation in the shade of green-blue and red shifted. In addition, it was noted that the AC conductivity conforms to the universal power law, establishing that load transport has been carried out by two conduction mechanisms: The NSPT for the low-frequency region and the CBH model for the high-frequency region. The temperature dependence of the DC conductivity and exponent factor was assessed employing the Arrhenius technique, confirming the results obtained for the conductivity. The large jump in activation energy and the change in the conduction mechanism can be explained by a change from proton conduction for $T < 363$ K to ionic conduction for $T > 363$ K. However, the frequency-dependent variations in the dielectric permittivity and modulus at different temperatures confirm the presence of two relaxation processes, attributed to the electrical response of the grains and grain boundaries of the investigated material. The analysis indicates that both relaxation processes, associated with the grains and grain boundaries, are thermally activated. Finally, the variation in L_n (ω_{max}) *versus* 1000/T reveals two relaxation regions with two activation energies, which aligns with the results obtained for the electrical conductivity.

Conflicts of interest

There are no conflicts to declare.

Data availability

CCDC 2281873 contain the supplementary crystallographic data for this paper.[95]

Supplementary information is available. See DOI: **https://doi.org/10.1039/d5ra07430d**.

Acknowledgements

The Minister of Superior Education and Research of Tunisia and the Spanish Ministerio de Ciencia e Innovación (PID2020-113558RB-C41) and Gobierno del Principado de Asturias (GRUPIN-2021/50997) are acknowledged.

References

1 M. Krimi, M. Akermi, R. Hassani and A. B. Rhaiem, *Solid State Sci.*, 2024, **155**, 107646.

2 I. Gueye, S. Ueda, A. Ogura and T. Nagata, *ACS Appl. Electron. Mater.*, 2024, **6**, 3237.
3 S. Feng, Q. Huang, S. Yang, Z. Lin and Q. Ling, *Chem. Sci.*, 2021, **12**, 14451.
4 Y. Liu, H.-T. Zhou, S.-P. Chen, Y.-H. Tan, C.-F. Wang, C.-S. Yang, H.-R. Wen and Y.-Z. Tang, *Dalton Trans.*, 2018, **47**, 3851.
5 O. Taktak, H. Souissi, I. Elhamdi, A. Oueslati, S. Kammoun, M. Gargouri and E. Dhahri, *Opt. Mater.*, 2024, **150**, 115251.
6 C.-Y. Mao, W.-Q. Liao, Z.-X. Wang, Z. Zafar, P.-F. Li, X.-H. Lv and D.-W. Fu, *Inorg. Chem.*, 2016, **55**, 7661.
7 I. Dakhlaoui, K. Karoui, F. Hajlaoui, N. Audebrand, T. Roisnel and F. Jomni, *J. Mol. Struct.*, 2021, **1231**, 129684.
8 S. Dgachi, M. M. Turnbull, F. Mezzadri, A. J. Norquist, A. Soran, J. Boonmak, G. Nemes and H. Naïli, *Inorg. Chim. Acta*, 2021, **514**, 119997.
9 J. Wu, N. Akhtar, R. Y. N. Gengler, T. T. M. Palstra and P. Rudolf, *J. Mater. Chem. C*, 2017, **5**, 1782–1788.
10 M. F. Mostafa, S. S. El-khiyami and S. K. Alal, *J. Phys. Chem. Solids*, 2018, **118**, 6.
11 X. Yu, T. J. Marks and A. Facchetti, *Nat. Mater.*, 2016, **15**, 383.
12 O. Guesmi, M. S. Abdelbaky, D. Martinez-Blanco, L. Ktari, S. Garcia-Granda and M. Dammak, *Inorg. Chim. Acta*, 2019, **496**, 119033.
13 M. Said and H. Boughzala, *J. Mol. Struct.*, 2019, **1189**, 122.
14 A. Kessentini, M. Belhouchet, J. J. Suñol, Y. Abid and T. Mhiri, *J. Mol. Struct.*, 2013, **1039**, 207.
15 D. Maraii and M. Dammak, Synthesis, *J. Mol. Struct.*, 2022, **1247**, 131282.
16 F. Bentahar, M. S. Abdelbaky, M. I. Menéndez, P. Huidobro, S. García-Granda and M. Dammak, *Polyhedron*, 2022, **228**, 116034.
17 F. Missaoui, M. Krimi, A. Mahmoud, F. Boschini and A. B. Rhaiem, *New J. Chem.*, 2024, **48**, 12817.
18 A. Moulahi, O. Guesmi, M. S. Abdelbaky, S. García-Granda and M. Dammak, *J. Alloys Compd.*, 2022, **898**, 162956.
19 P. Peksa and A. Sieradzki, *Lith. J. Phys.*, 2022, **62**, 195.
20 T. Tanzina, Investigation of the structural, electrical and magnetic properties of mn-doped AlFeO3, , PhD thesis*Bangladesh University of Engineering and Technology*, 2021, **http://lib.buet.ac.bd:8080/xmlui/handle/123456789/6081**.
21 E. Taflan, H. Bayrak, M. Er, Ş. A. Karaoğlu and A. Bozdeveci, *Bioorg. Chem.*, 2019, **89**, 102998.
22 Y.-S. Liu, Z.-K. Xu, J.-M. Zhang, X.-G. Chen, Y. Qin and Z.-X. Wang, *Dalton Trans.*, 2025, **54**, 4706.
23 H. Zhang, Z.-K. Xu, Z.-X. Wang, H. Yu, H.-P. Lv, P.-F. Li, W.-Q. Liao and R.-G. Xiong, *J. Am. Chem. Soc.*, 2023, **145**, 4892.
24 Y. Zeng, X. Huang, C. Huang, H. Zhang, F. Wang and Z. Wang, *Angew. Chem., Int. Ed.*, 2021, **60**, 10730.
25 M. M. Abdelkader, M. Abdelmohsen and A. I. Aboud, *Chem. Phys. Lett.*, 2021, **770**, 138423.
26 S. Walha, N. Mhadhbi, B. F. Ali, A. Kaiba, A. Guesmi, W. A. El-Fattah, N. B. Hamadi, M. M. Turnbull, F. Costantino and H. Naïli, *Chem. Phys. Impact*, 2024, **8**, 100597.
27 M. Said and H. Boughzala, *J. Mol. Struct.*, 2020, **1203**, 127413.
28 F. Issaoui, Y. Baklouti, E. Dhahri, F. Zouari and M. A. Valente, *J. Supercond. Novel Magn.*, 2015, **28**, 2621.
29 F. Issaoui, W. Amamou, M. Bekri, F. Zouari, E. Dhahri and M. A. Valente, *J. Mol. Struct.*, 2019, **1189**, 175.
30 A. Gannouni, I. Dridi, S. Elleuch, L. Jouffret and R. Kefi, *J. Mol. Struct.*, 2022, **1250**, 131804.
31 S. Chaouachi, B. Hamdi and R. Zouari, *Synth. Met.*, 2017, **223**, 122.
32 S. Trabelsie, A. Samet, H. Dammak, F. Michaud, L. Santos, Y. Abid and S. Chaabouni, *Opt. Mater.*, 2019, **89**, 355.
33 H. Khachroum, M. Krimi, M. S. Abdelbaky, S. García-Granda and M. Dammak, *Mater. Res. Bull.*, 2024, **179**, 112978.
34 M. Heine, L. Fink and M. U. Schmidt, *CrystEngComm*, 2020, **22**, 2067.
35 M. C. Burla, R. Caliandro, M. Camalli, B. Carrozzini, G. L. Cascarano, L. De Caro, C. Giacovazzo, G. Polidori, D. Siliqi and R. Spagna, *J. Appl. Crystallogr.*, 2007, **40**, 609.
36 L. J. Farrugia, WinGX and ORTEP for Windows: an update, *J. Appl. Crystallogr.*, 2012, **45**, 849.
37 O. V. Dolomanov, L. J. Bourhis, R. J. Gildea, J. A. K. Howard and H. Puschmann, *J. Appl. Crystallogr.*, 2009, **42**, 339.
38 G. M. Sheldrick, *Acta Crystallogr., Sect. C:Struct. Chem.*, 2015, **71**, 3.
39 K. Brandenburg, *Diamond–Crystal and Molecular Structure Visualization, version 3.2*, Crystal Impact, H, Putz K Brandenbg, GbR Bonn Ger., 2007, vol. 102, p. 53227.
40 C. F. Macrae, P. R. Edgington, P. McCabe, E. Pidcock, G. P. Shields, R. Taylor, M. Towler and J. V. D. Streek, *J. Appl. Crystallogr.*, 2006, **39**, 453.
41 A. Gannouni, I. Dridi, S. Elleuch, L. Jouffret and R. Kefi, *J. Mol. Struct.*, 2022, **1250**, 131804.
42 A. Tounsi, B. Hamdi, R. Zouari and A. B. Salah, *Phys. E*, 2016, **84**, 384.
43 F. Issaoui, W. Amamou, M. Bekri, F. Zouari, E. Dhahri and M. A. Valente, *J. Mol. Struct.*, 2019, **1189**, 175.
44 R. Moreno-Fuquen, C. Arana and C. A. De Simone, *Acta Crystallogr., Sect. E:Struct. Rep. Online*, 2012, **68**, o2805.
45 K. I. Hardcastle, M. J. Laing, T. J. McGauley and C. F. Lehner, *J. Cryst. Mol. Struct.*, 1974, **4**, 305.
46 M. Laing, N. Sparrow and P. Sommerville, *Acta Crystallogr., Sect. B*, 1971, **27**, 1986.
47 J. Karpagam, N. Sundaraganesan, S. Sebastian, S. Manoharan and M. Kurt, *J. Raman Spectrosc.*, 2010, **41**, 53.
48 M. Faizan, S. A. Bhat, M. J. Alam, Z. Afroz and S. Ahmad, *J. Mol. Struct.*, 2017, **1148**, 89.
49 M. F. Farona and N. J. Bremer, *J. Am. Chem. Soc.*, 1966, **88**, 3735.
50 K. Singh, S. Kapoor, R. Sachar, V. K. Gupta and R. Kant, *J. Crystallogr.*, 2014, **2014**, 1.
51 P. C. Ford and R. E. Clarke, *Chem. Commun.*, 1968, 1109.
52 M. M. Dirtu, C. Neuhausen, A. D. Naik, A. Leonard, F. Robert, J. M. Brynaert, B.-L. Su and Y. Garcia, *Cryst. Growth Des.*, 2011, **11**, 1375.
53 R. Yankova, Synthesis, Spectral Characteristics and DFT Studies of the [Cu (3-Amino-1, 2, 4-triazole) 3 SO 4], *Synthesis*, 2016, **2**, 15.

54 Y. Sert, *Pamukkale Univ Muh Bilim Derg.*, 2018, **24**, 1272.
55 I. X. J. Wang, X. Y. Qiao, Li Zi-Yan, D. H. Wei and Y. Y. Niu, *Inorg. Chem. Commun.*, 2020, **119**, 108.
56 J. Janczak and R. Kubiak, Synthesis, thermal stability and structural characterisation of iron(II) phthalocyanine complex with 4-cyanopyridine, *Polyhedron*, 2007, **13**, 2997.
57 S. Dgachi, F. Rahmouni, A. Soran, M. Saoudi, G. Nemes and H. Naïli, *J. Mol. Struct.*, 2021, **1244**, 130996.
58 S. Trabelsie, A. Samet, H. Dammak, F. Michaud, L. Santos, Y. Abid and S. Chaabouni, *Opt. Mater.*, 2019, **89**, 355.
59 V. V. Kovalev, Yu. E. Gorbunova, G. A. Razgonyaeva, S. A. Kozyukhin and Yu. V. Kokunov, *Russ. J. Coord. Chem.*, 2014, **40**, 801.
60 D. Sun, Z.-H. Wei, C.-F. Yang, D.-F. Wang, N. Zhang, R.-B. Huang and L.-S. Zheng, *CrystEngComm*, 2011, **13**, 1591.
61 R. Babu, A. K. Vardhaman, V. M. Dhavale, L. Giribabu and S. P. Singh, *Chem. Commun.*, 2019, **55**, 6779.
62 M. Said and H. Boughzala, *J. Mol. Struct.*, 2020, **1203**, 127413.
63 G. Stanescu and A. Trutia, *J. Optoelectron. Adv. Mater.*, 2005, **7**, 1009.
64 S. Chaouachi, S. Elleuch, B. Hamdi and R. Zouari, *J. Mol. Struct.*, 2016, **1125**, 149.
65 N. H. Buttrus, J. M. Alyass and A. F. Mohammad, *J. Chem. Chem. Eng.*, 2013, **7**, 613.
66 M. Ghedini, M. L. Deda, I. Aiello and A. Grisolia, *J. Chem. Soc., Dalton Trans.*, 2002, 3406.
67 H. Ben Attia, F. Bentahar, M. S. Abdelbaky, A. Elferjani, S. García-Granda and M. Dammak, *J. Alloys Compd.*, 2023, **969**, 172317.
68 F. S. Howell, R. A. Bose, P. B. Macedo and C. T. Moynihan, *J. Phys. Chem.*, 1974, **78**, 639.
69 M. F. Mostafa, S. S. El-khiyami and S. K. Alal, *J. Phys. Chem. Solids*, 2018, **118**, 6.
70 A. Ghoudi, I. Chaabane, R. Naouari, A. Aydi, A. Oueslati, E. Dhahri, B. F. O. Costa, T. Nikitin, J. A. Paixão and R. Fausto, *Inorg. Chem. Commun.*, 2024, 112925.
71 N. Mahfoudh, K. Karoui, M. Gargouri and A. BenRhaiem, *Appl. Organomet. Chem.*, 2020, **34**, e5404.
72 C. M. Zhu, G. B. Yu, L. G. Wang, M. W. Yao, F. C. Liu and W. J. Kong, Dielectric relaxation and magnetodielectric effect in the spinel NiCr2O4, *J. Magn. Magn. Mater.*, 2020, **506**, 166803.
73 D. Abid, I. Mjejri, A. Oueslati, P. Guionneau, S. Pechev, N. Daro and Z. Elaoud, *ACS Omega*, 2024, **9**, 12743.
74 A. K. Jonscher, The 'universal'dielectric response, *Nature*, 1977, **267**, 673.
75 C. B. Mohamed, K. Karoui, S. Saidi, K. Guidara and A. B. Rhaiem, *Phys. B*, 2014, **451**, 87.
76 A. Ghosh, *Phys. Rev. B:Condens. Matter Mater. Phys.*, 1990, **42**, 5665.
77 G. E. Pike and C. H. Seager, *J. Appl. Phys.*, 1979, **50**, 3414.
78 R. Salam, *Phys. Status Solidi A*, 1990, **117**, 535.
79 S. A. Yerişkin, G. E. Demir, İ. Yücedag and J. Nanoelectron, *Optoelectron.*, 2019, **14**, 1126.
80 A. Tataroglu, H. Durmuş, A. F. Vahid, B. Avar and Ş. Altındal, *J. Mater. Sci.:Mater. Electron.*, 2024, **35**, 227.
81 Y. Chen, S.-P. Zhao, J.-L. Liu, W.-H. Ning, X.-M. Sun and X.-M. Ren, *RSC Adv.*, 2014, **4**, 9178.
82 bC. Elissalde and J. Ravez, *J. Mater. Chem.*, 2001, **11**, 1957.
83 H. Fricke, *J. Phys. Chem.*, 1953, **57**, 934.
84 C. G. Koops, *Phys. Rev.*, 1951, **83**, 121.
85 K. Alberi, B. Fluegel, H. Moutinho, R. G. Dhere, J. V. Li and A. Mascarenhas, *Nat. Commun.*, 2013, **4**, 2699.
86 B. Barış, H. G. Özdemir, N. Tuğluoğlu, S. Karadeniz, Ö. F. Yüksel and Z. Kişnişci, *J. Mater. Sci.:Mater. Electron.*, 2014, **25**, 3586.
87 M. Ahmad, M. A. Rafiq, Z. Imran, K. Rasool, R. N. Shahid, Y. Javed and M. M. Hasan, *J. Appl. Phys.*, 2013, **114**, 043710.
88 P. Thongbai, S. Tangwancharoen, T. Yamwong and S. Maensiri, *J. Phys.:Condens. Matter*, 2008, **20**, 395227.
89 A. Tounsi, B. Hamdi, R. Zouari and A. B. Salah, *Phys. E*, 2016, **84**, 384.
90 N. Mahfoudh, K. Karoui and A. BenRhaiem, *RSC Adv.*, 2021, **11**, 24526.
91 S. A. Khan, F. S. Al-Hazmi, S. Al-Heniti, A. S. Faidah and A. A. Al-Ghamdi, *Curr. Appl. Phys.*, 2010, **10**, 145.
92 N. Murali, S. J. Margarette, V. K. Rao and V. Veeraiah, *J. Sci.:Adv. Mater. Devices*, 2017, **2**, 233.
93 A. Hunt, Non-Debye relaxation and the glass transition, *J. Non-Cryst. Solids*, 1993, **160**, 183.
94 F. Alvarez, A. Alegría and J. Colmenero, *Phys. Rev. B: Condens. Matter Mater. Phys.*, 1993, **47**, 125.
95 CCDC 2281873, Experimental Crystal Structure Determination, 2025, DOI: **10.5517/ccdc.csd.cc2glgtc**.